

in Biology and Medicine

Elsevier Editorial System(tm) for Computers

Manuscript Draft

Manuscript Number:

Title: Left ventricle Hermite-based segmentation

Article Type: Full Length Article

Keywords: Active shape models; steered Hermite transform; left ventricle segmentation; level sets; ray feature error

Corresponding Author: Mrs. Jimena Olveres, M.E.

Corresponding Author's Institution: UNAM

First Author: Jimena Olveres, M.Eng.

Order of Authors: Jimena Olveres, M.Eng.; Rodrigo Nava, Ph.D.; Boris Escalante-Ramírez, Ph.D.; Enrique Vallejo, M.D.; Jan Kybic, Ph.D.

Abstract: In recent years, computed tomography (CT) has become a standard technique in cardiac studies because it provides detailed images of human organs that may help to improve the diagnosis of the conditions that interfere with the proper operation of the heart. In this paper, we propose a novel multi-technique approach to segment endocardium and epicardium boundaries in CT. The proposal computes visually relevant information of the left ventricle and its adjacent structures using the Hermite transform and combines it with active shape models and level sets to improve the segmentation. We use 28 cardiac CT volumes manually segmented by expert physicians to validate the proposal and four-fold cross-validation to reduce bias. The assessment of the segmentation is computed using Dice index and Hausdorff distance. In addition, we introduce a novel metric called "ray feature error" to evaluate the segmentation performance. The results show that the proposal accurately discriminates cardiac tissue; thus, it may be useful for the support of diagnosis and treatments.

Suggested Reviewers: Rangaraj M. Rangayyan Ph.D.

Professor,, Department of Electrical and Computer Engineering, University of Calgary

ranga@ucalgary.ca

Expert on the field

Leo Joskowik Ph.D.

Head, Computer-Assisted Surgery and Medical Image Processing Laboratory, School of Computer Science and Engineering, The Hebrew University of Jerusalem

josko@cs.huji.ac.il

Expert on the field

Gabriel Cristobal Ph.D.

Professor, Optics Institute, CSIC

gabriel@optica.csic.es

Expert on the field

Opposed Reviewers:

## \*Conflict of Interest Statement

**Conflict of interest:** None of the authors has any conflict of interest. The authors have no personal financial or institutional interest in any of the materials, software or devices described in this article.

# Left ventricle Hermite-based segmentation

Jimena Olveres<sup>a,\*</sup>, Rodrigo Nava<sup>b</sup>, Boris Escalante-Ramírez<sup>c</sup>, Enrique Vallejo<sup>d</sup>, and Jan Kybic<sup>b</sup>

<sup>a</sup>*Posgrado en Ciencia e Ingeniería de la Computación, Universidad Nacional Autónoma de México, Mexico*

<sup>b</sup>*Faculty of Electrical Engineering, Czech Technical University in Prague, Czech Republic*

<sup>c</sup>*Facultad de Ingeniería, Universidad Nacional Autónoma de México, Mexico*

<sup>d</sup>*Hospital Angeles Pedregal, Mexico*

---

## Abstract

In recent years, computed tomography (CT) has become a standard technique in cardiac studies because it provides detailed images of human organs that may help to improve the diagnosis of the conditions that interfere with the proper operation of the heart. In this paper, we propose a novel multi-technique approach to segment endocardium and epicardium boundaries in CT. The proposal computes visually relevant information of the left ventricle and its adjacent structures using the Hermite transform and combines it with active shape models and level sets to improve the segmentation. We use 28 cardiac CT volumes manually segmented by expert physicians to validate the proposal and four-fold cross-validation to reduce bias. The assessment of the segmentation is computed using Dice index and Hausdorff distance. In addition, we introduce a novel metric called “ray feature error” to evaluate the segmentation performance. The results show that the proposal accurately discriminates cardiac tissue; thus, it may be useful for the support of diagnosis

---

\*Corresponding author.

*Email address:* `jolveres@uxmcc2.iimas.unam.mx` (Jimena Olveres)

and treatments.

*Keywords:* Active shape models, steered Hermite transform, left ventricle segmentation, level sets, ray feature error

---

## 1. Introduction

According to the World Health Organization, cardiovascular diseases (CVDs) rank number one as cause of death worldwide and were responsible for 31% of all deaths in 2012 [1]. CVDs are generally characterized by a blockage of blood vessels that does not allow part of the heart muscle to receive blood flow, which may lead to an acute myocardial infarction (AMI) or a stroke. Although sex, age, and race are related to heart failures; tobacco, unhealthy diet, and obesity also represent a major risk factor for AMI [2]. The estimated cost for CVDs and strokes in the United States during 2011 reached \$320.1 billions; it cost more than any other diagnostic group [3].

Conditions that interfere with the proper operation of the left ventricle (LV) are considered forms of CVDs. Some cardiomyopathies may cause LV to lose its ability to contract or relax normally. As a consequence, the heart cannot pump or fill with blood. In response, LV compensates for this stress by modifying its behavior, which creates a hypertrophy that causes enlargement and hardening of the LV muscle and progresses to a congestive heart failure [4]. Follow-up medical checkups and clinical controls increase the probability of survival of patients [5]. Thus, early detection of LV disorders has gained attention in the cardiology community [6].

Information about the current state of anatomical structures of the heart is needed for an early and accurate diagnosis. The most common modality for cardiac analysis is ultrasound-echocardiography mainly because of its low cost and good spatial resolution. Nevertheless, it depends on an acoustic window that causes large variability. Magnetic resonance imaging (MRI) has also been used as a reference method [7]. It is useful for the scanning

and detection of abnormalities in soft organs and there is no involvement of any kind of radiation yet it is pretty expensive compared with computed tomography (CT) [8].

On the other hand, CT imaging provides insights and detailed information of the heart to support and tailor treatments. Furthermore, heart examination using CT generates 2D and 3D high-resolution images throughout the entire cardiac cycle, which are useful for segmentation tasks.

As a prerequisite for LV visualization, the heart must be oriented in order to obtain a canonical view: horizontal, long, and short axis views. Short axis view shows a plane that is perpendicular to the long axis and gives a suitable cross-sectional view of both ventricles [6, 9]. On the short axis view, LV is displayed as an alignment from the base of the heart to the apex and is particularly appropriate for the assessment of volumetric measurements, ejection fraction, and myocardial mass (see Figure 1). Strain rate, which is defined as a change in the myocardial tissue length, can also be evaluated on this view [7]. Note that the aforementioned parameters are quantified only after the segmentation of the LV.

Several techniques have been developed for epicardium and endocardium segmentation in the short axis view. In [10], Petitjean and Dacher presented a review of a large group of automated and semi-automated segmentation methods that includes those based on atlases, deformable models, pixel classification, region and edge detectors, and active shape models. However, these methods are focused on MRI.

Although CT imaging does not provide suitable contrast resolution in comparison with MRI, it is far more accessible and has enough spatial resolution

to distinguish adjacent organs [11].

To the best of our knowledge, there is a limited number of scientific papers addressing CT-based heart segmentation. For instance, Funka-Lea et al. [12] proposed an automatic heart segmentation method in CT using graph-cuts. Jolly et al. [13] also used graph-cuts and the expectation maximization algorithm to segment myocardium in 4D cardiac MRI and CT, but finding the optimal cost-cut may cause the procedure stops at local minimum. Region growing and threshold methods have been used to assess the ventricular function and for quantification of pericardial fat [14, 15]. Nevertheless, these methods are sensitive to initialization, noise, and image characteristics.

Ecabert et al. [16] addressed heart segmentation using active shape models (ASMs) but it requires a large training set in order to compensate problems such undefined boundaries, noise, and lack of contrast. Zheng et al. [17] presented an improvement of the previous algorithm to localize heart chambers with steerable filters. Kang et al [7] presents a review about the most used methods on cardiac segmentation. However, classic active contours and level sets are associated with a minimum, which often leads to over-segmentation [18].

Due to the complexity of the segmentation tasks, other studies have suggested that the combination of different techniques may improve organ segmentation [19, 20, 21, 22].

In [23] the authors combined well-known segmentation methods with fitting algorithms to improve the results. Also in [24], the authors used a combined approach based on local binary patterns (LBPs) and ASMs to segment the mesencephalon. The results have shown that such a combination



outperforms single approaches.

LBPs are also proven to be a suitable tool when they are used in combination with active contours because LBPs are able to model local structures in a robust way against illumination changes, while ASMs take advantage of the velocity of local variations to localize landmarks [25]. In addition, features such as texture, color, or morphology should be included in a deeper analysis in order to enhance the performance of the final segmentation [26].

On the other hand, methods that resemble the human visual system have increased in popularity because they allow to expand images into local decompositions that describe intrinsic attributes related to important cues and highlight structures useful for segmentation purposes [27]. In particular, the Hermite transform (HT) [28, 29] has been used successfully as a texture descriptor [30, 31]. HT is a special case of the Polynomial transform; it is based on Gaussian derivatives and allows us to compute local orientation analysis.

Cardiac segmentation is still a challenging task due to biological aspects that depend on the organ anatomy diversity and physical issues that image modalities must face. For example, noise from the respiratory system and unwanted movements, cardiac synchronization, and differences in anatomy when a pathology occurs.

In this paper, we propose a novel multi-technique strategy to segment LV boundaries with more precision. This strategy includes a combination of information produced by HT with ASM and LS approaches, therefore, the proposal takes advantage of the relevant perceptual information about LV and its adjacent structures to improve the segmentation. This procedure

considers endocardium (inner wall) and epicardium (outer wall) delineations.

Although papillary muscles are typically excluded, here we also consider them in our segmentation approach. Such a consideration may allow to measure the total volume of blood throughout the entire cardiac cycle. Specifically, we conduct several evaluations using Dice coefficient, Hausdorff distance, and also introduce a novel metric called "ray feature error" (see Appendix A). Furthermore, we include a comparison between our proposal and different schemes based on ASMs, LBPs, and LS.

The remainder of the paper is organized as follows: Section 2 presents the mathematical foundations; in Section 3 the dataset is described; in Section 4, under the hypothesis that combined methods may improve LV segmentation, we introduce our proposal; in Section 5 the experiments are shown; finally, Section 6 concludes the paper addressing unresolved challenging problems.

## 2. Theoretical Background

In this section, we briefly present the mathematical foundations that are used in this proposal.

### 2.1. Active shape models

In [32], Cootes et al. proposed active shape models as a refinement of statistical deformable models. An ASM consists of an average shape,  $\bar{X}$ , that is derived from a point distribution model (PDM). The goal of the approach relies on the idea that it is possible to deform  $\bar{X}$  to some extent in order to produce certain variability until the ASM meets the boundaries of the object of interest. The algorithm includes also a gray-level appearance model. It is divided into the following steps:

- 125 (i) A set of  $M$  aligned shapes is built. For each training shape, a vector of landmarks is obtained:  $S_i = \{(x_0, y_0), \dots, (x_{i-1}, y_{i-1})\}^T$ . So that, the average shape is the mean of all landmarks  $\bar{X} = \frac{1}{M} \sum_{k=0}^{M-1} S_k$ .
- (ii) Single value decomposition is used to find the PDM parameters. The least significant eigenvalues and eigenvectors are removed to avoid  
130 singular correlation matrix and data over-fitting [24].
- (iii) The mean shape is deformed within certain limits to recognize a new shape as follows:

$$\hat{X} = \bar{X} + P\mathbf{b} \quad (1)$$

where  $\bar{X}$  is the average shape,  $P$  is the matrix of the  $t$  first principal components,  $\mathbf{b}$  is the weight vector, and  $\hat{X}$  is the estimated shape. Eq.  
135 (1) is know as PDM.

- (iv)  $\bar{X}$  is placed close to the object of interest manually. Each landmark in  $\bar{X}$  is compared against its corresponding profile, which is a line of pixels that is perpendicular to the landmark. Then, the landmarks are moved iteratively towards those that obtain the lowest distance to the desired  
140 contour. The process is iterative and stops when a specific number of iterations or a threshold is reached.

## 2.2. Deformable models based on level sets

Nowadays, a multitude of deformable models based on level set exists in the literature. However, the Chan-Vese model [33] is one of the best known  
145 algorithms.

Let  $u_0$  be an image such that  $u_0 : \Omega \rightarrow \mathbb{R}$ . Then, the objective of the Chan-Vese model is to minimize an energy functional and finds a partition  $C$  that forms a border between two regions of interest in  $u_0$ . The model is useful when an image does not contain well-defined boundaries; furthermore,  
 150 it is less sensitive to noise.

An extension of this model also exists, called vector-value model [34] where complimentary information of the image can be considered to obtain an improved segmentation.

This model minimizes the energy functional using the Euler-Lagrange  
 155 equation:

$$\frac{\partial \phi}{\partial t} = \delta_\epsilon \left[ \mu \operatorname{div} \left( \frac{\nabla \phi}{|\nabla \phi|} \right) - \frac{1}{N} \sum_{i=1}^N \lambda_i^+ (u_{0,i} - c_i^+)^2 + \frac{1}{N} \sum_{i=1}^N \lambda_i^- (u_{0,i} - c_i^-)^2 \right] \quad (2)$$

$c^+$  and  $c^-$  are constant vectors that represent the average value of  $u_0$  inside and outside the curve  $C$ , respectively.  $\mu$  and  $\lambda^{+,-}$  allow to tune the object detector sensitivity. However, this method is computationally demanding [35, 36].

160 In this paper, we use a model called fast level set (FLS) [37], which is a variation of the classic Chan-Vese algorithm. FLS aims to improve performance and reduce computational complexity by avoiding the iterative solution of the partial differential equation, Eq. (2). It has a simple discrete representation that reduces computational complexity. The idea of FLS is to  
 165 represent the zero level set as a list of boundary points that moves towards a discrete edge without computing Eq. (2). At the same time, FLS preserves the advantages of traditional methods.

Further simplifications come from the the fact that the evolution of FLS needs binary information that derives into a speed function  $v(x)$  as follows:

$$v(x) = \begin{cases} 1 & \text{if } -\lambda_1(f(x) - c_1)^2 + \lambda_2(f(x) - c_2)^2 \geq 0 \\ -1 & \text{if } -\lambda_1(f(x) - c_1)^2 + \lambda_2(f(x) - c_2)^2 < 0 \end{cases} \quad (3)$$

170

The algorithm includes a regularization phase with an anisotropic Gaussian filter applied to the level set function.

FLS is a reliable algorithm. However, the main drawback is that the initial regions must be well defined in order to create the initial speed.

### 175 2.3. *Steered Hermite Transform*

Over the last decades, many computational methods have incorporated simple biological properties of vision. One example is the Hermite transform [28] that allows performing local orientation analysis by windowing an image with a Gaussian function. On each window position, an expansion using orthogonal polynomials is calculated; such an expansion is called steered Hermite coefficients (HCs).

180

The importance of HT relies on the fact that its characteristics mimic receptive fields of the human visual system and extract relevant image structures efficiently [38, 39].

185

HT is associated with a class of orthogonal polynomials called Hermite polynomials,  $H_n(x)$ , defined as follows:

$$H_n(x) = (-1)^n e^{x^2} \frac{d^n (e^{-x^2})}{dx^n} \quad (4)$$

where  $n$  denotes the order of the polynomial.

The Cartesian Hermite coefficients,  $L_{n-m,m}$ , can be directly obtained by convolving the image,  $I(x, y)$ , with the Hermite analysis functions,  $D_n$ , (see Figure 2(a)) as follows:

$$L_{n-m,m}(x_0, y_0) = \iint I(x, y) D_{n-m,m}(x_0 - x, y_0 - y) dx dy \quad (5)$$

with  $D_n(x) = H_n(x) \cdot G^2(x)$  where  $G^2(x)$  represents a Gaussian function.

The steered Hermite transform (SHT) is derived from a linear combination of rotated Cartesian Hermite coefficients [40] (see Figure. 2(b)). The rotation follows a maximum energy criteria [27]. SHT produces a new and reduced set of HCs oriented over the angle  $\theta$ :

$$L_{m,n-m,\theta}(x_0, y_0) = \sum_{k=0}^n L_{k,n-k}(x_0, y_0) R_{k,n-k}(\theta) \quad (6)$$

where  $R_{m,n-m}(\theta) = \sqrt{\binom{n}{m}} \cos^m(\theta) \sin^{n-m}(\theta)$ .

SHT has proven to be effective in texture analysis [40, 27]. It is well suitable for multi-resolution analysis and can be implemented as a fast algorithm [40].

### 3. Materials

A dataset of 28 annotated tomographic cardiac studies in healthy subjects was taken with a CT Siemens dual source scanner (128 channels) at Hospital Ángeles Pedregal México. The volumes were captured in signed 12-bits DICOM format without any personal information.

Each study belongs to a unique subject and consisted of 10 volumes taken at different times during the electrocardiography (ECG)-synchronized cardiac cycle. This method is called ECG-gating where a volume is acquired only during certain consecutive period of the cardiac cycle; it covers systolic and diastolic cardiac phases. Our studies start on a final diastolic (relaxing) phase,

go throughout the systolic (contraction) phase and return to the diastolic  
210 phase, providing images at 0%, 10%, 20%, 30%, 40%, 50%, 60%, 70%, 80%  
and 90% of the cardiac cycle. The spatial resolution values range from  
 $0.302734 \times 0.302735 \times 1.5$  [mm] to  $0.433593 \times 0.433593 \times 1$  [mm].

Since the volumes are oriented on different angles, an alignment with the  
short axis view was performed. Thus, it was necessary to rotate at least two  
215 of the axes and apply translations (see Figure 3). This step was reviewed  
by experienced physicians. Furthermore, due to the fact that modern CT  
scanners have a wide range of Hounsfield units (HU), the volumes were mapped  
into a more suitable range from -1024HU to 2200HU. Then, a normalization  
step was applied to avoid negative values.

## 220 4. Methodology

The objective of this study is to identify with a better precision endocardial  
and epicardial walls that contain myocardium.

In our dataset the endocardium possesses good contrast, while the epi-  
cardium is not always well-defined. Several attempts to segment such struc-  
225 tures have been made but still better techniques are needed to improve results.  
As mentioned in section 1 deformable models such as ASMs and active con-  
tours based on LS have been intensely used on the ventricle segmentation.  
We suggest to take advantage of the SHT to characterize important tissue  
structures and incorporate them into the ASMs and LS schemes to improve  
230 the segmentation. A block diagram resumes the proposal in Figure 4.

The first step is to seed a suitable initialization for the ASM and LS  
algorithms. This is accomplished by estimating the position of the centroid

of the LV blood pool using a compactness metric during the diastole phase (see Figure 5). This is a simple yet effective way to compute the initial pose. We perform this step on the middle slices of the volumes. A limitation is that in the case of failure, the LV cavity center must be manually specified.

#### 4.1. Combining active shape models

We propose to combine ASMs and HCs to improve the segmentation of the LV. In addition, we made changes to the original ASM algorithm and explore four methods. For all cases, the initial parameters are set to: number of landmarks = 70, normal profile length = 11, and search iterations = 60.

##### 4.1.1. **ASM/HCs**

First, the HCs using Eq. (6) are computed and then incorporated into the ASM in a multi-spectral fashion. Namely, every steered Hermite coefficient vector  $\{L_k | k = 0, \dots, 3\}$  is considered a multi-spectral band. Thus, the multi-spectral values of the landmarks and profiles,  $g_i$ , are defined as follows:

$$g_i = \begin{bmatrix} g_{pL_0}(x_p, y_p : L_0), g_{pL_1}(x_p, y_p : L_1), \dots, \\ g_{pL_2}(x_p, y_p : L_2), g_{pL_3}(x_p, y_p : L_3) \end{bmatrix} \quad (7)$$

where  $g_{pL_k}$  are the gray values at the position  $(x, y)$  that correspond to the profile  $p$  of the HCs  $L_0, L_1, L_2$ , and  $L_3$  respectively. Here, we use the Mahalanobis distance to calculate the closest point to the landmark.

##### 4.1.2. **ASM/Profile-HCs**

For every landmark and their corresponding profile, the HCs are computed over a  $9 \times 9$  pixel window. The final histogram is built by concatenating the



histograms of all the HCs (see Figure 6).

$$p(r_{kL_n}) = \frac{1}{MN} \{n_{kL_0}, n_{kL_1}, n_{kL_2}, n_{kL_3}\} \quad (8)$$

#### 4.1.3. *ASM/Quadratic-HCs*

255 Here, we propose to compute HCs over four square regions around landmarks defined by a  $7 \times 7$  pixel window. According to our results, this method outperforms ASM/Quadratic-LBP (see Figure 7).

$$p(r_{QkL_n}) = \frac{1}{MN} \{n_{QkL_0}, n_{QkL_1}, n_{QkL_2}, n_{QkL_3}\} \quad (9)$$

#### 4.1.4. *ASM/Quadratic-LBP*

In [24], the authors proposed to combine ASMs and LBPs by considering  
 260 only profiles of landmarks (see Figure 8(a)). Here, we extend the area of analysis. During the training phase, LBPs are calculated over four square regions of  $5 \times 5$  pixels around the landmarks, then a histogram is built by concatenating the four local histograms to describe the corresponding landmark (see Figure 8(b)). LBP is a simple powerful method to describe textures.  
 265 Despite the fact that there are quite a few versions [41], here, we opted for the original LBP because of its good performance and simplicity.

In the recognition phase, the previous procedure is performed over all the profiles. The resulted histograms are compared against the histogram of the corresponding landmark, so that, the closest point to the boundary is the one  
 270 with the smallest histogram distance. Here, we used Chi-square distance. A diagram with the description of the method is shown in Figure 8.

## 4.2. Combining fast level sets

Level sets are an efficient method for segmenting organ tissue when the borders possess good contrast as in the case of the endocardium. However, the main bottleneck is the computation time. Thus, we use fast level sets in combination with the Hermite coefficients. After testing with several iteration values we studied the behavior of the number of iterations vs. the error, in order to obtain the best value, the final value for number of iterations is 60.

### 4.2.1. FLS/HCs

The steered Hermite coefficients are used as a simplified vector model that defines the initial velocity field as follows:

$$\begin{aligned} \frac{\partial \phi}{\partial t} = \delta_\epsilon \left[ \mu \operatorname{div} \left( \frac{\nabla \phi}{|\nabla \phi|} \right) - \frac{1}{4} \left\{ \lambda_0^+ (L_0 - c_0^+)^2 + \lambda_1^+ (L_1 - c_1^+)^2 \right. \right. \\ \left. \left. + \lambda_2^+ (L_2 - c_2^+)^2 + \lambda_3^+ (L_3 - c_3^+)^2 \right\} \right. \\ \left. + \frac{1}{4} \left\{ \lambda_0^- (L_0 - c_0^-)^2 + \lambda_1^- (L_1 - c_1^-)^2 \right. \right. \\ \left. \left. + \lambda_2^- (L_2 - c_2^-)^2 + \lambda_3^- (L_3 - c_3^-)^2 \right\} \right] \end{aligned} \quad (10)$$

where  $L_x$  are the HCs,  $C_x^-$  are the average values inside the curve  $C$ , and  $C_x^+$  represent average values outside the curve.

## 5. Experimental results

The aforementioned algorithms were validated against manual annotations made by expert physicians in 28 studies throughout the entire cardiac cycle from different healthy subjects.

We used the middle slices of the volumes, so that, every study was composed of ten images, which covered diastole and systole phases. We also identified each slice with the percentage of the cardiac cycle [0%, 10%, 20%, ..., 90%]. In conjunction a total of 280 different images were tested.

In order to reduce bias, we used four-fold cross-validation to train the ASM. Every fold was chosen randomly. Our experiments were divided into two groups: Endocardium (Section 5.1) and epicardium segmentation (Section 295 5.2).

Experiments with fast level sets include an expansion of the resulted contour that encloses the cavity segmentation. The procedure segments papillary muscles followed by a convex hull in order to generate a rounded envelope to enfold them (see Figure 9(a)). This step represents a refinement 300 of the segmentation that allows us to resemble boundaries manually drawn by clinicians.

On the other hand, in the case of ASM-based segmentation, only the algorithm approximation was used (see Figure 9(b)). Therefore, we compared blue contours against ground-truth boundaries in red.

305 Regarding steered Hermite coefficient computation, different window sizes were evaluated. However, the window of size of  $9 \times 9$  pixels achieved better quantitative results.

We performed a quantitative analysis using three metrics: (i) Hausdorff distance (HD); (ii) Dice index (DI); and (iii) Ray feature error (RFE). RFE 310 is a novel metric for segmentation evaluation based on ray features [42]. It allows us to measure in a simple and robust way shape similarities between two overlapping objects. The method is introduced in Appendix A. Examples of the best segmentation cases for endocardium and epicardium are shown in Figure 10(a) and Figure 10(b), respectively.

315 *5.1. Endocardium segmentation*

Seven different schemes were computed. Two methods using fast level sets: FL and FL/HCs; and five methods using ASM-based schemes: ASM, ASM/HCs, ASM/Profile-HCs, ASM/Quadratic-HCs, and ASM/Quadratic-LBP.

320 The best results were achieved with FL and FL/HCs, while ASM/Quadratic-LBP presents the worst results. Since level set-based algorithm performance strongly depends on the number of iterations, then we include a comparison of the two best algorithms and their behavior when the number of iterations changes (see Figure 11 and Figure 12). The average results are resumed in  
325 Figure 13, Figure 14, and Figure 15 using HD, DI, and RFE respectively.

*5.2. Epicardium segmentation*

Six different approaches were computed: FL/HCs, ASM, ASM/HCs, ASM/Profile-HCs, ASM/Quadratic-HCs, and ASM/Quadratic-LBP. In this section we did not include FL because the algorithm did not converge due to  
330 the lack of contrast.

ASM/Quadratic-HCs outperformed all the methods, whereas ASM/HCs achieved the poorest results. The average results are resumed in Figure 16, Figure 17, and Figure 18 using HD, DI, and RFE respectively.

Segmentation of endocardium and epicardium throughout the cardiac  
335 cycle is presented in Figure 19.

## 6. Conclusions and future work

In this work, we have implemented a semi-automatic segmentation method for the left ventricle on the short axis view throughout the entire cardiac

cycle. Due the tomographic image qualities, we used different approaches  
340 based on region characteristics. Thus, we explored the performance of two  
types of deformable models: Active shape models and level sets. Hermite  
features help to improve the segmentation, specially when we deal with noise  
and lack of contrast.

We consider fast level sets as a first option when endocardium is segmented  
345 because border tissues are well-defined. Notice from Figure 11 and Figure  
12 that the results when FL is combined with HCs are better because the  
information given from HCs controls the speed function.

ASMs in combination with Hermite coefficients also improved the endo-  
cardium segmentation. Notice how ASM/Profile-HCs and ASM/Quadratic-  
350 HCs maintain second places on the bar graphs (see Figures 13, 14, and 15)  
mainly because the image expansion with the steered Hermite transform  
allows us to extract features based on Gaussian derivatives that highlight  
salient visual cues. The steered Hermite transform enhances segmentation  
because it adapts to local orientation content.

355 As we mentioned before, the window of analysis used to compute the  
steered Hermite coefficients was set to  $9 \times 9$  on all algorithms. We evaluated  
different sizes:  $5 \times 5$ ,  $7 \times 7$ , and  $11 \times 11$  with suboptimal results. Nevertheless  
the Hermite window size is not related with the LBP window used because  
in both cases they belong to a different analysis and also the LBP size was  
360 previously evaluated and taken from the results shown on the paper [24]  
where multiple variations of LBPs were studied.

Regarding epicardium segmentation, fast level sets are not presented in this  
study because they never converge due to the lack of contrast. Nevertheless,

when Hermite coefficients and fast level sets were used in combination, the  
365 epicardium segmentation significant improved in spite of poor contrast.

Even more, the combination of HCs and ASMs also improved the perfor-  
mance on the epicardium, and to this matter, the contribution of the shape  
restriction, inherent to the method, also benefits. Important to mention is  
that in other variations of ASMs like in the case of adding Hermite coeffi-  
370 cients and LBP information, the algorithm behavior also improved, specially  
in the case of using a local approach such as in ASM/Quadratic-HCs and  
ASM/Quadratic-LBP, which suggests that not only adding the coefficients is  
enough, but also using this coefficients as part of a regional approach.

From result tables we can infer that in most cases the segmentation  
375 algorithm changes its error performance when dealing with a systole or  
diastole phase.

The segmentation of the left ventricle presented in this work constitutes  
a way of understanding the complex heart dynamics. The obtained results  
resemble clinical delineations in CT imaging and prove that the methods may  
380 help to reduce bias in diagnosis and treatment procedures.

In the last part of this study, we introduced a novel method to assess  
contour-based segmentation called ray feature error. This method is a simple  
way to estimate border errors in a range  $[0, 1)$ . Since the error is anywhere  
between zero and one, it gives an estimation of the magnitude of the error

385 Future work should include datasets with cardiomyopathies and 3D im-  
plementation of the best methods. Also a further analysis must be conducted  
to obtain quantitative LV parameters such as ejection percentage that is  
essential for all medical diagnosis.

## A. Ray feature error

390 Since active contours have become a popular technique frequently used in image segmentation, it is necessary to use a metric that allows us to assess their performance objectively. Here, we propose a fast and robust yet simple method for quantitative evaluation of contour-based segmentation called ray feature error (see Figure 20). RFE is based on the original proposal of 395 ray features [42] where authors compute four image features to characterize irregular shapes: Distance difference, distance feature, orientation, and norm feature.

RFE allows measuring shape similarities between two overlapping objects as follows:

- 400 • Given two closed objects  $A$  and  $B$ , we define the location  $C_{AB}$  as the common centroid of both objects.
- It is possible to calculate the distance from the location  $p$  in  $A$  to the nearest border in the direction of  $\theta$  as follows:

$$dA_{\theta}(p, \theta) = \|f(A, p, \theta) - p\| \quad (11)$$

where  $f(A, p, \theta)$  returns the location of the nearest border to  $p$  in  $A$  in 405 the direction of  $\theta$  and  $\|\bullet\|$  is the Euclidean norm.

- The local error between two objects in the direction of  $\theta$  is obtained as the absolute value of the difference of the distances:

$$E(AB)_{\theta} = |dA_{\theta} - dB_{\theta}| \quad (12)$$

- Finally, RFE is computed as:

$$RFE(A, B) = \frac{\sum_{\theta} |dA_{\theta} - dB_{\theta}|}{DA + DB} \quad (13)$$

where  $DX = \sum_{\theta} dX_{\theta}$ .

410 REF represents a simple and fast way to compare two overlapping closed shapes. It varies within the range  $[0, 1)$  and  $RFE(A, B) = 0$  if and only if A and B have the closure,  $A = B$ .

## Acknowledgments

This work has been sponsored by UNAM grant PAPIIT IG100814. Also,  
 415 it was partially supported by the European social fund within the project CZ.1.07/2.3.00/30.0034. R. Nava and J. Olveres thank Consejo Nacional de Ciencia y Tecnología (CONACYT). J. Kybic was supported by the Czech Science Foundation project 14-21421S.

## References

- 420 [1] World Health Organization (WHO), [Cardiovascular diseases \(CVDs\), fact sheet](#), accessed: 2016-04-20 (2015).  
 URL <http://www.who.int/mediacentre/factsheets/fs317/en/>
- [2] S. Ye, Acute myocardial infarction, in: M. D. Gellman, J. R. Turner (Eds.), *Encyclopedia of Behavioral Medicine*, Springer New York, New York, NY, 2013, pp. 27–29. doi:10.1007/978-1-4419-1005-9\_1243.
- 425



- [3] D. Mozaffarian, E. J. Benjamin, A. S. Go, D. K. Arnett, M. J. Blaha, M. Cushman, S. de Ferranti, J.-P. Després, H. J. Fullerton, V. J. Howard, M. D. Huffman, S. E. Judd, B. M. Kissela, D. T. Lackland, J. H. Lichtman, L. D. Lisabeth, S. Liu, R. H. Mackey, D. B. Matchar, D. K. McGuire, E. R. Mohler, C. S. Moy, P. Muntner, M. E. Mussolino, K. Nasir, R. W. Neumar, G. Nichol, L. Palaniappan, D. K. Pandey, M. J. Reeves, C. J. Rodriguez, P. D. Sorlie, J. Stein, A. Towfighi, T. N. Turan, S. S. Virani, J. Z. Willey, D. Woo, R. W. Yeh, M. B. Turner, [on behalf of the American Heart Association Statistics Committee and Stroke Statistics Subcommittee. Heart disease and stroke statistics-2015 Update: a report from the American Heart Association.](#), accessed: 2016-08-29 (2015). [doi:10.1161/CIR.000000000000157](#).  
URL <http://circ.ahajournals.org/content/131/4/434>
- [4] R. Ventura-Clapier, *Encyclopedia of Exercise Medicine in Health and Disease*, Springer Berlin Heidelberg, 2012, Ch. Cardiomyopathies, pp. 175–175. [doi:10.1007/978-3-540-29807-6\\_4103](#).
- [5] S. Leschka, S. Waelti, S. Wildermuth, Principles of CT imaging, in: F. Saremi (Ed.), *Cardiac CT and MR for Adult Congenital Heart Disease*, Springer, New York, 2014, pp. 77–105.
- [6] U. J. Schoepf, C. R. Becker, L. K. Hofmann, Y. E. Kent, Multidetector-row CT of the heart, *Radiologic Clinics* 42 (3) (2004) 635–649. [doi:10.1016/j.rcl.2004.03.011](#).
- [7] D. Kang, J. Woo, P. J. Slomka, D. Dey, G. Germano, C.-C. Jay Kuo,

- Heart chambers and whole heart segmentation techniques: Review,  
450 Journal of Electronic Imaging 21 (1) (2012) 010901–1–010901–16.
- [8] P. C. e. a. Moschetti K, Muzzarelli S, Cost evaluation of cardiovascular  
magnetic resonance versus coronary angiography for the diagnostic work-  
up of coronary artery disease: Application of the european cardiovascular  
magnetic resonance registry data to the german, united kingdom, swiss,  
455 and united states health care systems, Journal of Cardiovascular Magnetic  
Resonance 14 (1) (2012) 35. [doi:10.1186/1532-429X-14-35](https://doi.org/10.1186/1532-429X-14-35).
- [9] R. Fischbach, Cardiac and cardiothoracic anatomy in CT, in: B. Ohne-  
sorge, T. Flohr, C. Becker, A. Knez, M. Reiser (Eds.), Multi-slice and  
Dual-source CT in Cardiac Imaging, Springer Berlin Heidelberg, 2007,  
460 pp. 23–39. [doi:10.1007/978-3-540-49546-8\\_2](https://doi.org/10.1007/978-3-540-49546-8_2).
- [10] C. Petitjean, J.-N. Dacher, A review of segmentation methods in short  
axis cardiac MR images, Medical Image Analysis 15 (2) (2011) 169–184.
- [11] S. Halliburton, A. Arbab-Zadeh, D. Dey, A. J. Einstein, R. Gentry,  
R. T. George, T. Gerber, M. Mahesh, W. G. Weigold, State-of-the-  
465 art in CT hardware and scan modes for cardiovascular CT, Journal  
of Cardiovascular Computed Tomography 6 (3) (2012) 154–163. [doi:  
10.1016/j.jcct.2012.04.005](https://doi.org/10.1016/j.jcct.2012.04.005).
- [12] G. Funka-Lea, Y. Boykov, C. Florin, M. P. Jolly, R. Moreau-Gobard,  
R. Ramaraj, D. Rinck, Automatic heart isolation for CT coronary vi-  
470 sualization using graph-cuts, in: 3rd IEEE International Symposium

on Biomedical Imaging: Nano to Macro, 2006., 2006, pp. 614–617.  
[doi:10.1109/ISBI.2006.1624991](https://doi.org/10.1109/ISBI.2006.1624991).

- [13] M.-P. Jolly, Automatic segmentation of the left ventricle in cardiac MR and CT images, *Int. J. Comput. Vision* 70 (2) (2006) 151–163.  
475 [doi:10.1007/s11263-006-7936-3](https://doi.org/10.1007/s11263-006-7936-3).
- [14] G. Mühlenbruch, M. Das, C. Hohl, J. E. Wildberger, D. Rinck, T. G. Flohr, R. Koos, C. Knackstedt, R. W. Günther, A. H. Mahnken, Global left ventricular function in cardiac CT. evaluation of an automated 3d region-growing segmentation algorithm, *European Radiology* 16 (5)  
480 (2006) 1117–1123. [doi:10.1007/s00330-005-0079-z](https://doi.org/10.1007/s00330-005-0079-z).
- [15] R. Yalamanchili, D. Dey, U. Kukure, R. Nakazato, D. S. Berman, I. A. Kakadiaris, Knowledge-based quantification of pericardial fat in non-contrast CT data, in: *Proc. SPIE Medical Imaging*, Vol. 7623, 2010, pp. 76231X–1–76231X–8. [doi:10.1117/12.843867](https://doi.org/10.1117/12.843867).
- 485 [16] O. Ecabert, J. Peters, J. Weese, Modeling shape variability for full heart segmentation in cardiac computed-tomography images, in: *Proc. SPIE Medical Imaging*, Vol. 6144, 2006, pp. 61443R–1–61443R–12. [doi:10.1117/12.652105](https://doi.org/10.1117/12.652105).
- [17] Y. Zheng, A. Barbu, B. Georgescu, M. Scheuering, D. Comaniciu,  
490 Fast automatic heart chamber segmentation from 3d CT data using marginal space learning and steerable features, in: *IEEE 11th International Conference on Computer Vision*, 2007, pp. 1–8. [doi:10.1109/ICCV.2007.4408925](https://doi.org/10.1109/ICCV.2007.4408925).

- [18] X. Bresson, S. Esedoglu, P. Vandergheynst, J.-P. Thiran, S. Osher,  
495 Fast global minimization of the active contour/snake model, *Journal of  
Mathematical Imaging and Vision* 28 (2) (2007) 151–167. doi:[10.1007/  
s10851-007-0002-0](https://doi.org/10.1007/s10851-007-0002-0).
- [19] Y.-L. Lu, K. A. Connelly, A. J. Dick, G. A. Wright, P. E. Radau,  
500 Automatic functional analysis of left ventricle in cardiac cine MRI,  
*Quantitative Imaging in Medicine and Surgery* 3 (4).
- [20] D. Turco, C. Corsi, *Advanced PDE-based Methods for Automatic Quan-  
tification of Cardiac Function and Scar from Magnetic Resonance Imaging.*  
Series in Computer Vision in Medical Imaging. Computer Vision: Volume  
2., World Scientific Publishing Company, University of Massachusetts,  
505 USA, 2013.
- [21] A. V. Juan J. Cerrolaza, R. Cabeza, *On Hierarchical Statistical Shape  
Models with application to Brain MRI.* Series in Computer Vision in Med-  
ical Imaging. Computer Vision: Volume 2, World Scientific Publishing  
Company, University of Massachusetts, USA, 2013.
- 510 [22] A. Kronman, L. Joskowicz, A geometric method for the detection and  
correction of segmentation leaks of anatomical structures in volumetric  
medical images, *International Journal of Computer Assisted Radiology  
and Surgery* 11 (3) (2016) 369–380. doi:[10.1007/s11548-015-1285-z](https://doi.org/10.1007/s11548-015-1285-z).
- [23] M. N. Bugdol, E. Pietka, [Mathematical model in left ventricle segmenta-  
515 tion](#), *Comput. Biol. Med.* 57 (C) (2015) 187–200.  
URL <http://dx.doi.org/10.1016/j.combiomed.2014.12.009>

- [24] J. Olveres, R. Nava, B. Escalante-Ramírez, G. Cristóbal, C. M. García-Moreno, Midbrain volume segmentation using active shape models and LBPs, in: Proc. SPIE Europe, Vol. 8856, 2013, pp. 88561F–1–88561F–11.
- 520 [25] J. Keomany, S. Marcel, Active shape models using local binary patterns, Tech. rep., IDIAP (2006).
- [26] J. Olveres, R. Nava, E. Moya-Albor, B. Escalante-Ramírez, J. Brieva, G. Cristóbal, E. Vallejo, Texture descriptor approaches to level set segmentation in medical images, in: Proc. SPIE Europe, Vol. 9138, 2014, pp. 91380J–91380J–12. [doi:10.1117/12.2054527](https://doi.org/10.1117/12.2054527).
- 525 [27] A. Estudillo-Romero, B. Escalante-Ramírez, Rotation-invariant texture features from the steered Hermite transform, Pattern Recognition Letters 32 (16) (2011) 2150–2162.
- [28] J.-B. Martens, The Hermite transform-theory, IEEE Transactions on Acoustics, Speech and Signal Processing 38 (9) (1990) 1595–1606.
- 530 [29] J.-B. Martens, The Hermite transform-applications, IEEE Transactions on Acoustics, Speech and Signal Processing 38 (9) (1990) 1607–1618.
- [30] Y. Wu, J. Shen, Properties of orthogonal Gaussian-Hermite moments and their applications, EURASIP Journal on Advances in Signal Processing 2005 (4) (2005) 1–12. [doi:10.1155/ASP.2005.588](https://doi.org/10.1155/ASP.2005.588).
- 535 [31] C. J. Rivero-Moreno, S. Bres, Texture feature extraction and indexing by Hermite filters, in: Proceedings of the 17th International Conference on Pattern Recognition, Vol. 1, 2004, pp. 684–687. [doi:10.1109/ICPR.2004.1334266](https://doi.org/10.1109/ICPR.2004.1334266).

- 540 [32] T. F. Cootes, C. J. Taylor, D. H. Cooper, J. Graham, Active shape models: their training and application, *Comput. Vis. Image Underst.* 61 (1) (1995) 38–59. [doi:10.1006/cviu.1995.1004](https://doi.org/10.1006/cviu.1995.1004).
- [33] T. Chan, L. Vese, Active contours without edges, *IEEE Transactions on Image Processing* 10 (2) (2001) 266–277. [doi:10.1109/83.902291](https://doi.org/10.1109/83.902291).
- 545 [34] T. F. Chan, B. Y. Sandberg, L. A. Vese, Active contours without edges for vector-valued images, *Journal of Visual Communication and Image Representation* 11 (2000) 130–141.
- [35] C. Li, C. Kao, J. Gore, Z. Ding, Implicit active contours driven by local binary fitting energy, in: *Proceedings of IEEE Conference on Computer Vision and Pattern Recognition (CVPR)*, 2007, pp. 1–7.
- 550 [36] B. X. Houhou Nawal, Thiran Jean-Philippe, Fast texture segmentation based on semi-local region descriptor and active contour, *Numerical Mathematics: Theory , Methods and Applications* 2 (2009) 445–468.
- [37] J. Kratky, J. Kybic, Three-dimensional segmentation of bones from CT and MRI using fast level sets, in: *Proc. SPIE Medical Imaging*, Vol. 6914, 555 2008, pp. 691447–1–691447–10.
- [38] T. Lindeberg, A computational theory of visual receptive fields, *Biological Cybernetics* 107 (6) (2013) 589–635. [doi:10.1007/s00422-013-0569-z](https://doi.org/10.1007/s00422-013-0569-z).
- [39] R. Young, R. Lesperance, W. W. Meyer, The Gaussian derivative model for spatial-temporal vision: I. cortical model, *Spatial Vision* 14 (3) (2001) 560 261–319. [doi:http://dx.doi.org/10.1163/156856801753253582](https://dx.doi.org/10.1163/156856801753253582).

- [40] J. L. Silván-Cárdenas, B. Escalante-Ramírez, The multiscale Hermite transform for local orientation analysis, *IEEE Transactions on Image Processing*. 15 (5) (2006) 1236–1253.
- 565 [41] R. Nava, G. Cristóbal, B. Escalante-Ramírez, A comprehensive study of texture analysis based on local binary patterns, in: *Proc. SPIE 8436, Optics, Photonics, and Digital Technologies for Multimedia Applications II*, 2012, pp. 84360E–1–84360E–12. [doi:10.1117/12.923558](https://doi.org/10.1117/12.923558).
- 570 [42] K. Smith, A. Carleton, V. Lepetit, Fast ray features for learning irregular shapes, in: *IEEE 12th International Conference on Computer Vision*, 2009, pp. 397–404. [doi:10.1109/ICCV.2009.5459210](https://doi.org/10.1109/ICCV.2009.5459210).

## List of Figures

575	1	CT image of the heart displayed using the short axis view where it is possible to see the right and left ventricles. The red ellipse defines the endocardium, whereas the blue ellipse defines epicardium. This segmentation resembles typical boundaries drawn by clinicians. . . . .	32
580	2	(a) Ensemble of spatial Hermite filters (left) and their corresponding frequency responses (right). We display orders from $N = 0$ to $N = 4$ . (b) Cartesian (left) and steered Hermite coefficients (right). Note that most coefficient energy is concentrated in the upper row of the steered Hermite coefficients.	33
585	3	CT dataset example. The original dataset was captured on different orientations. Therefore, the slices were preprocessed, so that, all images are aligned with the short axis view. Images taken (a) before and (b) after the alignment. . . . .	34
590	4	Overview of the experiments conducted in this study. First, feature extraction is performed and then incorporated into both ASMs and LS methods to improve segmentation of cardiac walls. The assessment is conducted with three metrics: Hausdorff, Dice, and, Ray feature error. . . . .	35
595	5	Metric of compactness. The blue numbers indicate the compactness value. A value of 1 means that the shape of the object is closer to a circle. During this step, we keep the object with the larger compactness value. . . . .	36
600	6	ASM/Profile-HCs scheme. The diagram shows the construction of the histogram for each landmark. For a given point in a profile the four histograms of the corresponding Hermite coefficients are concatenated. . . . .	37
605	7	ASM/Quadratic-HCs scheme. The diagram shows the construction of the histogram. For a given point, four regions on every Hermite coefficient are considered to build the histogram.	38
	8	Two different ways to combine ASMs and LBPs. (a) For every landmark, the LBP histograms are computed on all points of the corresponding profile of length $n$ . (b) Quadratic-LBP histogram computes LBPs on four square regions of $5 \times 5$ pixels around each landmark, then a histogram is built by concatenating the four local histograms one after another. . .	39



610	9	(a) Endocardium segmentation with fast level sets that includes papillary muscles (yellow); convex hull (blue); and manual segmentation (red). After cavity segmentation, a refinement is conducted in order to generate contours that resemble the expert ground truth. (b) Epicardium segmentation ASM (blue) and its corresponding manual contour segmentation (red). . . .	40
615	10	Segmentation details. Expert contour (red), algorithm result (blue). Best segmentation cases for (a) HEQ algorithm on the epicardium and (b) FL/HCs algorithm on the endocardium, it includes the contour (yellow) delineating papillary muscles. . . .	41
620	11	Dice index endocardium segmentation using FL and FL/HCs methods. The plots depict performance of the algorithms when the number of iterations are changed. The values were taken during (a) 0%, (b) 30%, (c) 60%, and (d) 90% of the cardiac cycle. . . . .	42
625	12	Ray feature error endocardium segmentation using FL and FL/HCs methods. The plots depict performance of the algorithms when the number of iterations are changed. The values were taken during (a) 0%, (b) 20%, (c) 50%, and (d) 90% of the cardiac cycle. . . . .	43
630	13	Average distances computed between the computed contour and the expert contour with Hausdorff distance for endocardium segmentation. X-axis represents the percentages during the cardiac cycle (diastole-systole). Note that lower values indicate more alike boundaries. . . . .	44
635	14	Average distances between the computed contour and the expert contour with Dice index for endocardium segmentation. X-axis represents the percentages during the cardiac cycle (diastole-systole). Note that values close to 1 indicate more similar contours. . . . .	45
640	15	Average distances between the computed contour and the expert contour with ray feature error for endocardium segmentation. X-axis represents the percentages during the cardiac cycle (diastole-systole). . . . .	46

645	16	Average distances between the computed contour and the expert contour with Hausdorff distance for epicardium segmentation. X-axis represents the percentages during the cardiac cycle (diastole-systole). Note that lower values indicate more alike boundaries. . . . .	47
650	17	Average distances between the computed contour and the expert contour with Dice index for epicardium segmentation. X-axis represents the percentages during the cardiac cycle (diastole-systole). Note that values close to 1 indicate more similar contours. . . . .	48
655	18	Average distances between the algorithm contour and the expert contour with ray feature error for epicardium segmentation. X-axis represents the percentages during the cardiac cycle (diastole-systole). . . . .	49
660	19	Final segmentations of endocardium (red), epicardium (blue), and papillary muscles (yellow) throughout the whole cardiac cycle. . . . .	50
660	20	Ray feature error method. Given two closed overlapping objects, RFE measures similarities between them by computing and adding $E_\theta$ with $\theta = \{0, \dots, 2\pi\}$ . . . . .	51

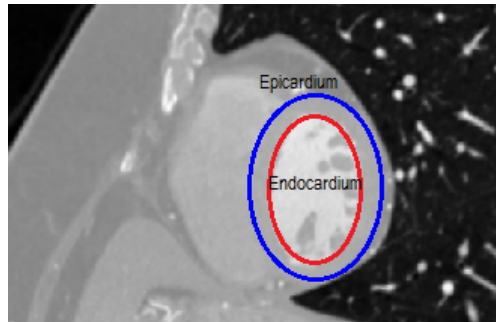
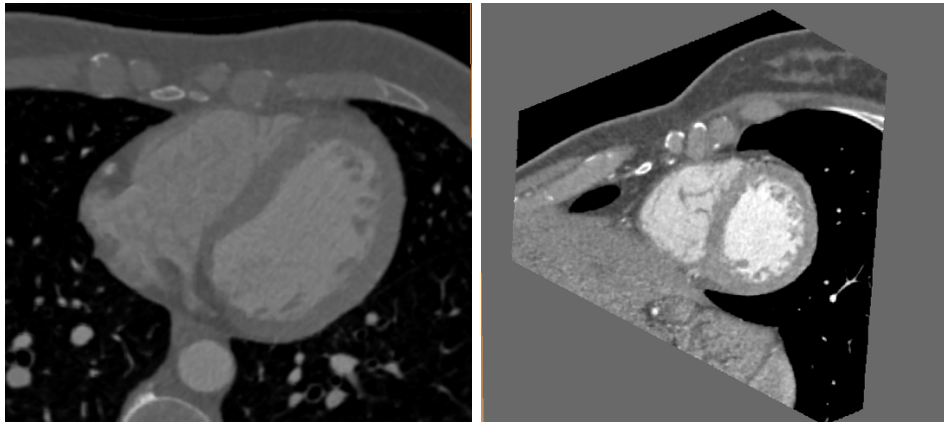


Figure 1: CT image of the heart displayed using the short axis view where it is possible to see the right and left ventricles. The red ellipse defines the endocardium, whereas the blue ellipse defines epicardium. This segmentation resembles typical boundaries drawn by clinicians.



Figure 2: **(a)** Ensemble of spatial Hermite filters (left) and their corresponding frequency responses (right). We display orders from  $N = 0$  to  $N = 4$ . **(b)** Cartesian (left) and steered Hermite coefficients (right). Note that most coefficient energy is concentrated in the upper row of the steered Hermite coefficients.



(a)

(b)

Figure 3: CT dataset example. The original dataset was captured on different orientations. Therefore, the slices were preprocessed, so that, all images are aligned with the short axis view. Images taken (a) before and (b) after the alignment.

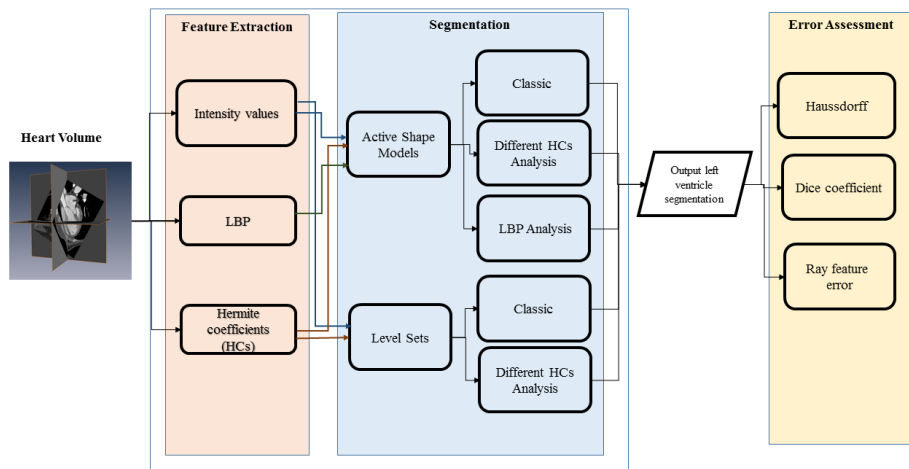


Figure 4: Overview of the experiments conducted in this study. First, feature extraction is performed and then incorporated into both ASMs and LS methods to improve segmentation of cardiac walls. The assessment is conducted with three metrics: Hausdorff, Dice, and, Ray feature error.

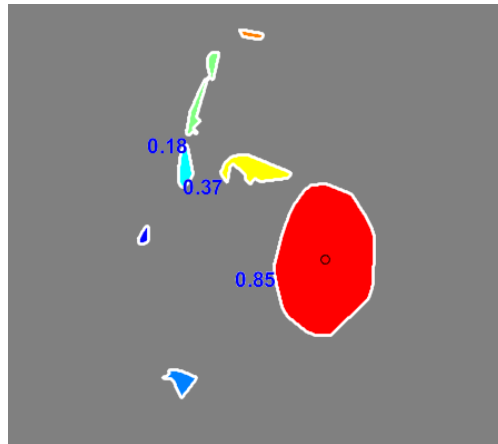


Figure 5: Metric of compactness. The blue numbers indicate the compactness value. A value of 1 means that the shape of the object is closer to a circle. During this step, we keep the object with the larger compactness value.

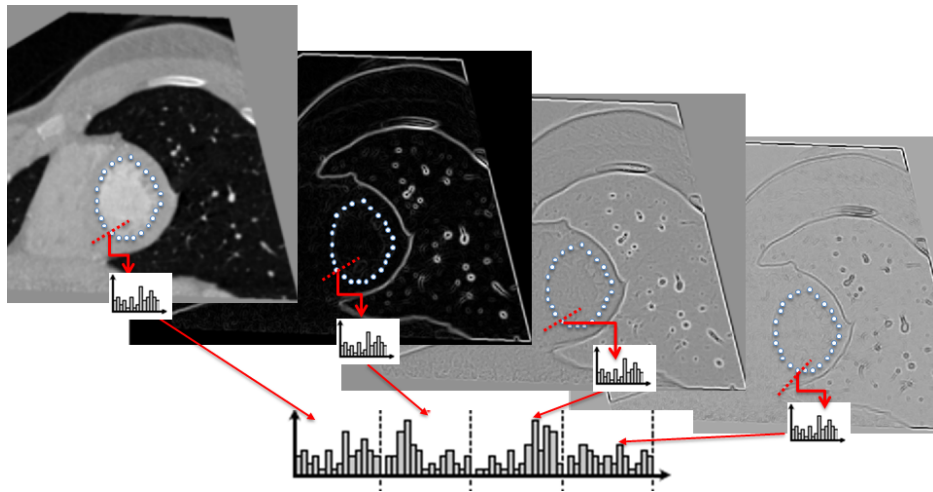


Figure 6: ASM/Profile-HCs scheme. The diagram shows the construction of the histogram for each landmark. For a given point in a profile the four histograms of the corresponding Hermite coefficients are concatenated.



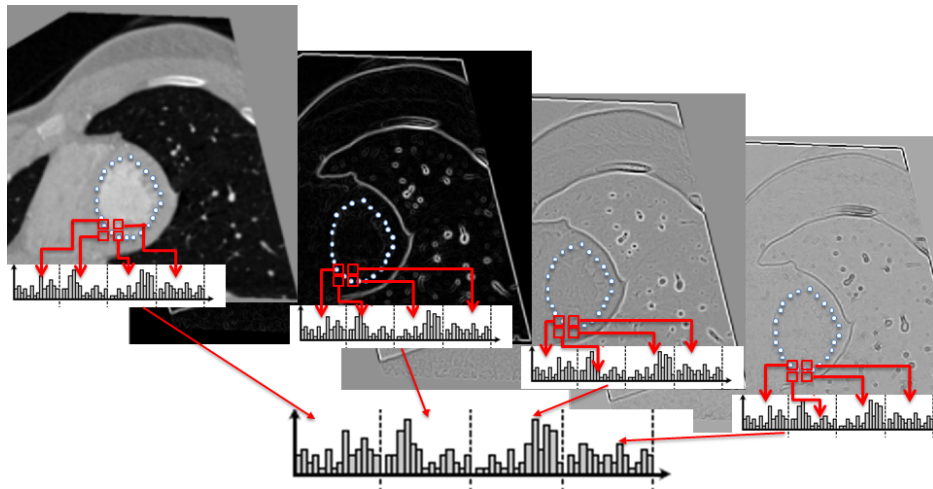


Figure 7: ASM/Quadratic-HCs scheme. The diagram shows the construction of the histogram. For a given point, four regions on every Hermite coefficient are considered to build the histogram.

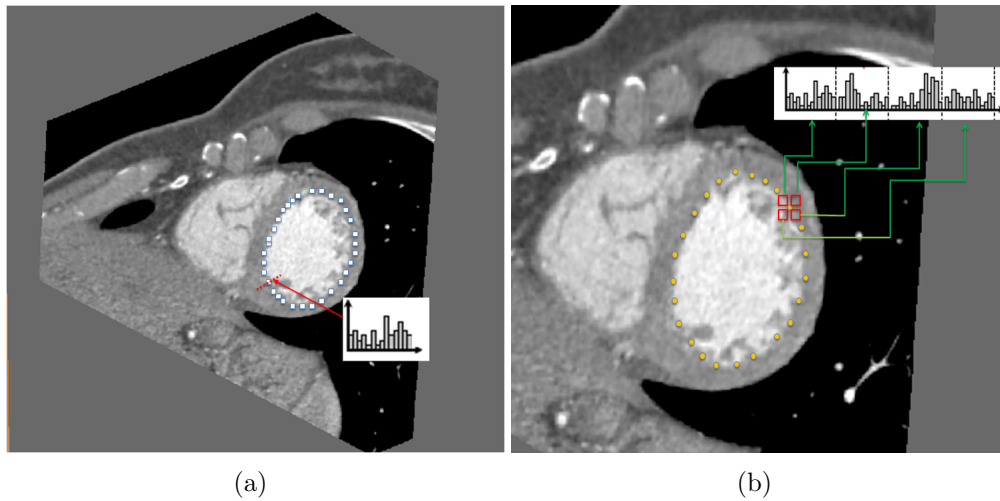


Figure 8: Two different ways to combine ASMs and LBPs. **(a)** For every landmark, the LBP histograms are computed on all points of the corresponding profile of length  $n$ . **(b)** Quadratic-LBP histogram computes LBPs on four square regions of  $5 \times 5$  pixels around each landmark, then a histogram is built by concatenating the four local histograms one after another.

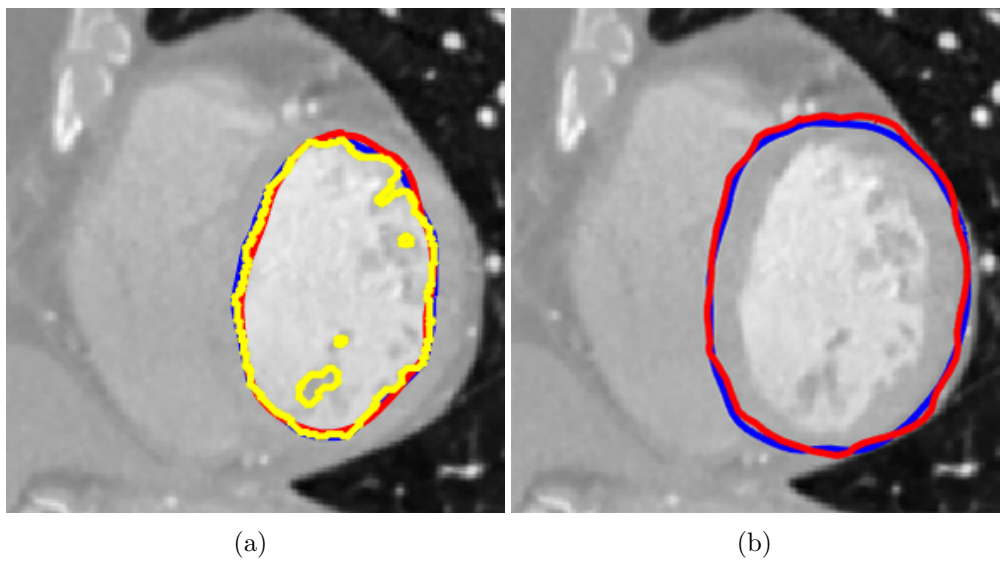


Figure 9: **(a)** Endocardium segmentation with fast level sets that includes papillary muscles (yellow); convex hull (blue); and manual segmentation (red). After cavity segmentation, a refinement is conducted in order to generate contours that resemble the expert ground truth. **(b)** Epicardium segmentation ASM (blue) and its corresponding manual contour segmentation (red).

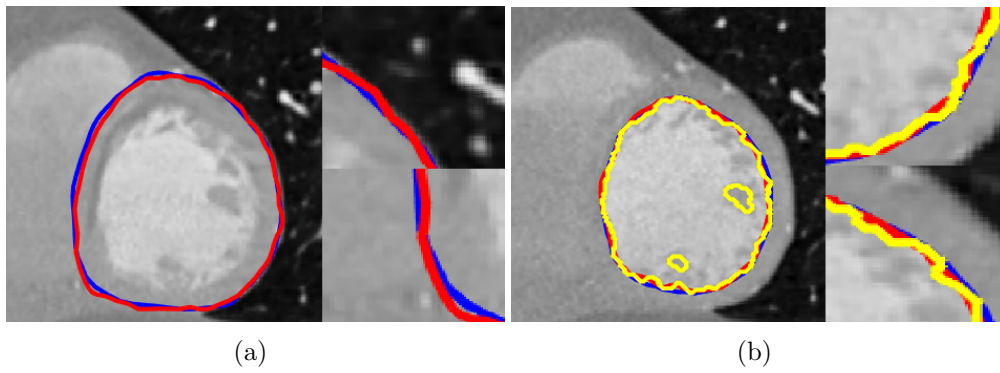


Figure 10: Segmentation details. Expert contour (red), algorithm result (blue). Best segmentation cases for **(a)** HEQ algorithm on the epicardium and **(b)** FL/HCs algorithm on the endocardium, it includes the contour (yellow) delineating papillary muscles.

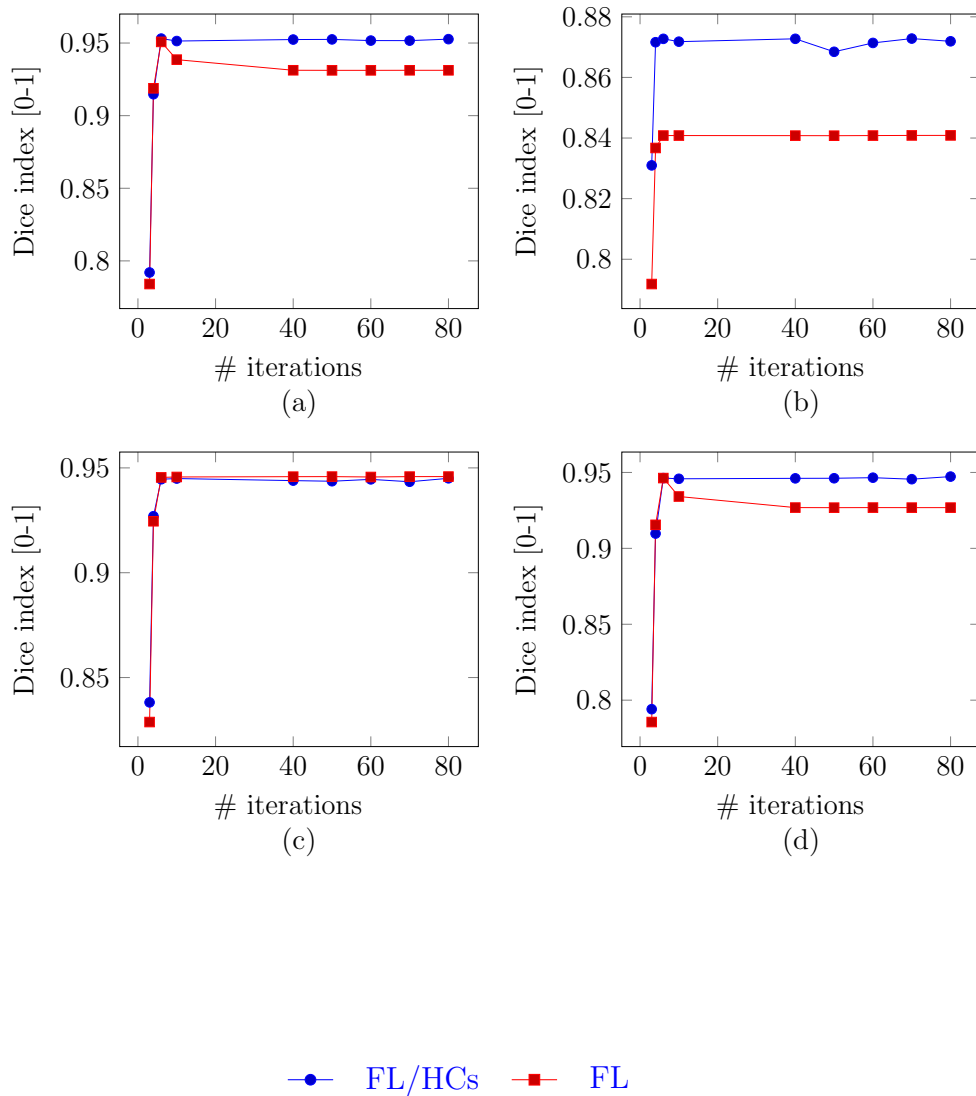


Figure 11: Dice index endocardium segmentation using FL and FL/HCs methods. The plots depict performance of the algorithms when the number of iterations are changed. The values were taken during (a) 0%, (b) 30%, (c) 60%, and (d) 90% of the cardiac cycle.

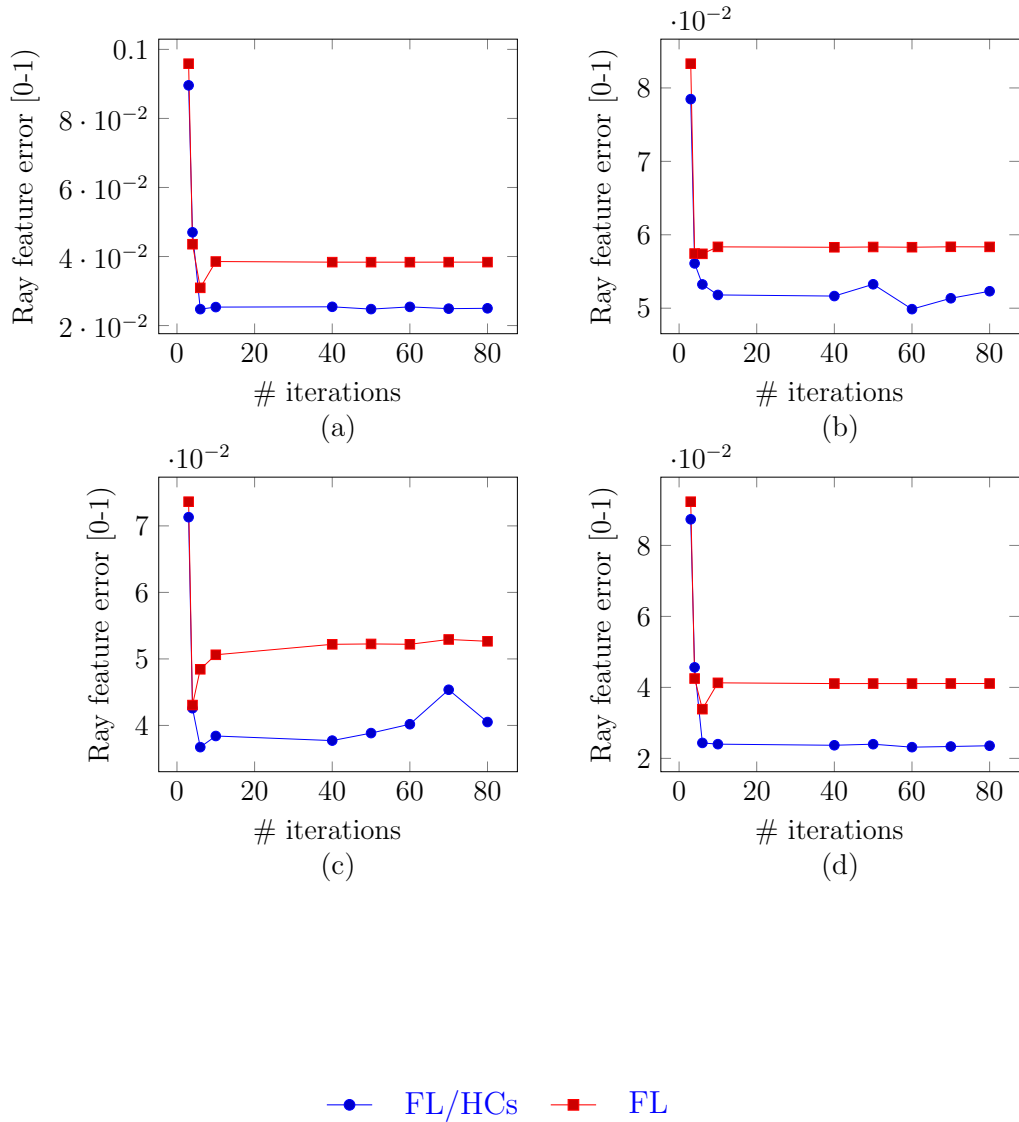


Figure 12: Ray feature error endocardium segmentation using FL and FL/HCs methods. The plots depict performance of the algorithms when the number of iterations are changed. The values were taken during (a) 0%, (b) 20%, (c) 50%, and (d) 90% of the cardiac cycle.

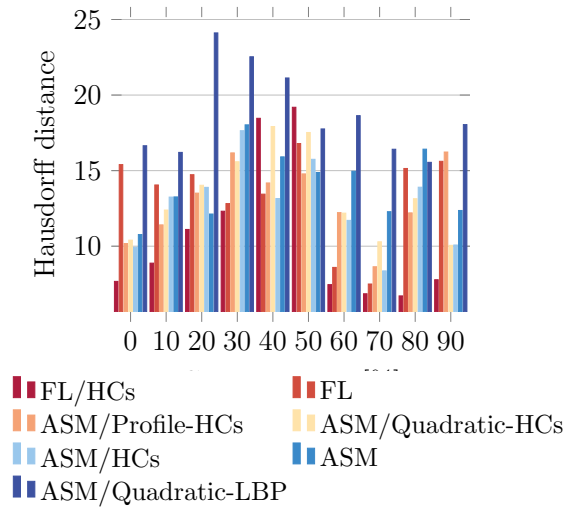


Figure 13: Average distances computed between the computed contour and the expert contour with Hausdorff distance for endocardium segmentation. X-axis represents the percentages during the cardiac cycle (diastole-systole). Note that lower values indicate more alike boundaries.

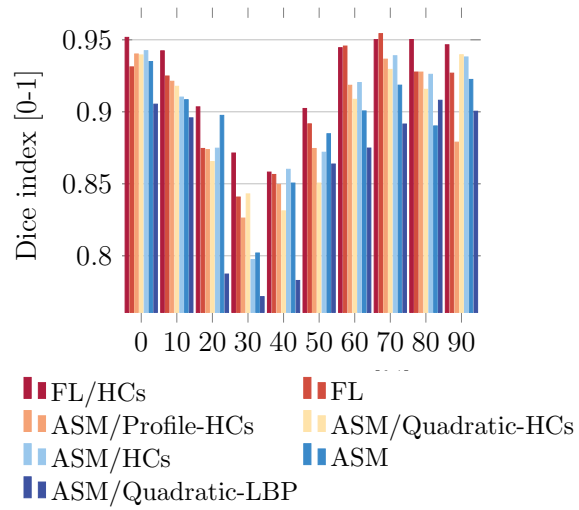


Figure 14: Average distances between the computed contour and the expert contour with Dice index for endocardium segmentation. X-axis represents the percentages during the cardiac cycle (diastole-systole). Note that values close to 1 indicate more similar contours.



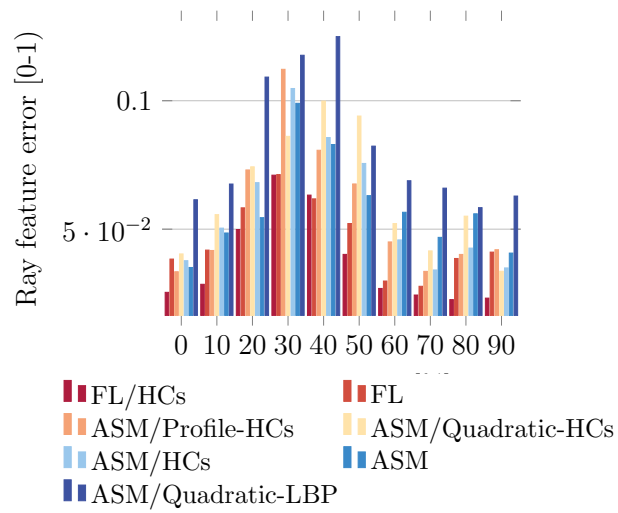


Figure 15: Average distances between the computed contour and the expert contour with ray feature error for endocardium segmentation. X-axis represents the percentages during the cardiac cycle (diastole-systole).

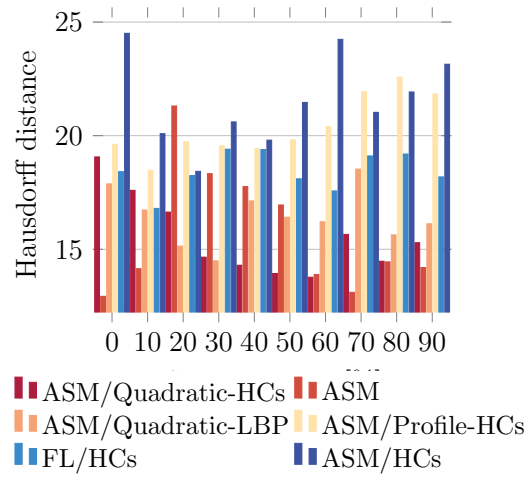


Figure 16: Average distances between the computed contour and the expert contour with Hausdorff distance for epicardium segmentation. X-axis represents the percentages during the cardiac cycle (diastole-systole). Note that lower values indicate more alike boundaries.

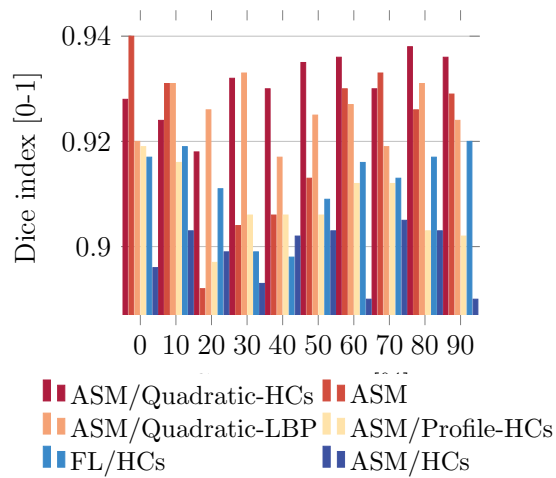


Figure 17: Average distances between the computed contour and the expert contour with Dice index for epicardium segmentation. X-axis represents the percentages during the cardiac cycle (diastole-systole). Note that values close to 1 indicate more similar contours.

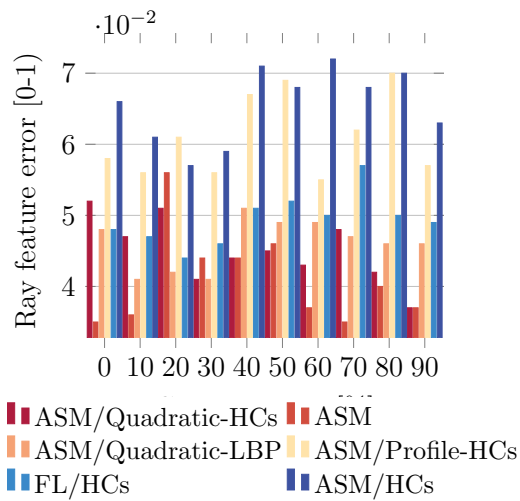


Figure 18: Average distances between the algorithm contour and the expert contour with ray feature error for epicardium segmentation. X-axis represents the percentages during the cardiac cycle (diastole-systole).

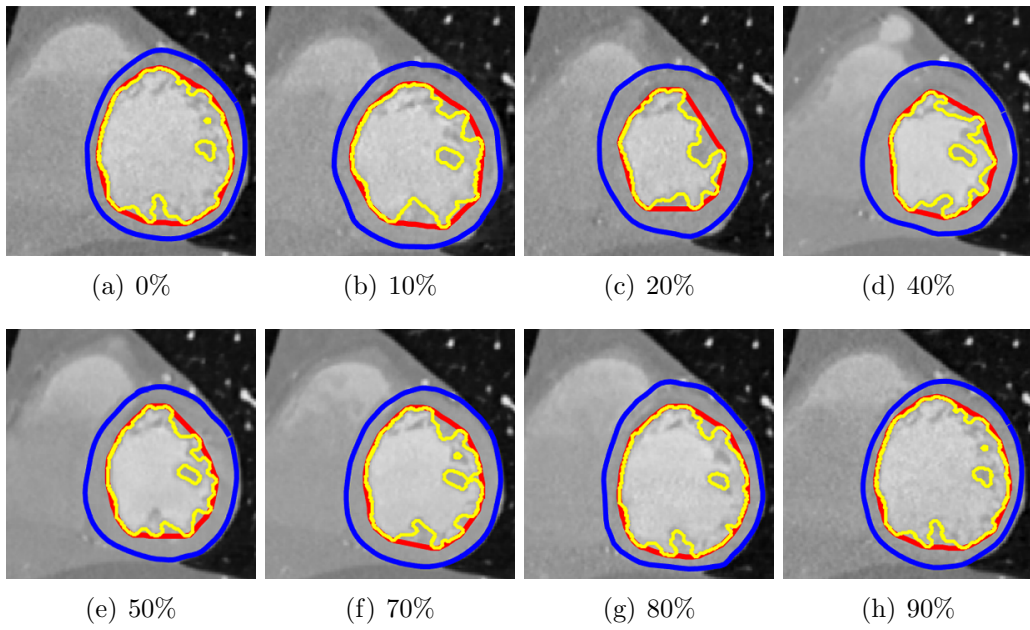


Figure 19: Final segmentations of endocardium (red), epicardium (blue), and papillary muscles (yellow) throughout the whole cardiac cycle.

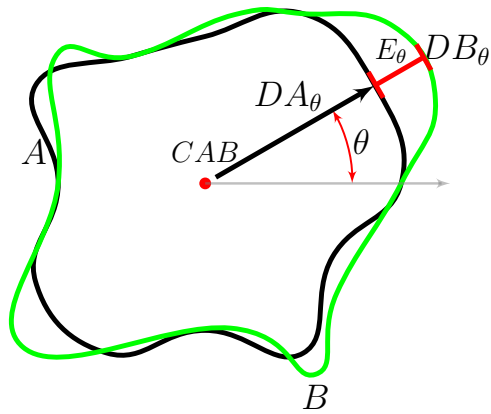


Figure 20: Ray feature error method. Given two closed overlapping objects, RFE measures similarities between them by computing and adding  $E_\theta$  with  $\theta = \{0, \dots, 2\pi\}$ .

### AUTHOR BIOGRAPHY

**Jimena Oliveres** received a Bachelor of Biomedical Engineering degree from the Universidad Iberoamericana A.C., a Master of Electrical Engineering degree and is a Ph.D. candidate at the Posgrado en Ciencia e Ingeniería en Computación from the Universidad Nacional Autónoma de México. She has been lecturing on medical image processing and computer vision at the Electrical Engineering Division of the School of Engineering. Her research interests are in computer vision, image processing, and segmentation.

**Rodrigo Nava** was born in Mexico City. He obtained the Bachelor of Computer Engineering degree in 2004; the Master of Computer Science and Engineering degree in 2007; and the Doctor of Engineering degree in 2013, all with honors, from the Universidad Nacional Autónoma de México. His research interests include bio-inspired image models, image fusion, image quality, and wavelets. He is a Candidate Member of the National Research System (CONACYT : 2015-2017)

**Boris Escalante-Ramírez** received a Bachelor of Electrical Engineering degree from Universidad Nacional Autónoma de México in 1985, a Master of Electronic Engineering degree from the Philips International Institute of Technological Studies, Eindhoven, The Netherlands, in 1987, and a Ph.D. degree from the Eindhoven University of Technology in 1992. Since then he has been with the Electrical Engineering Division of the School of Engineering, Universidad Nacional Autónoma de México.

**Enrique Vallejo** was born in Mexico City. He holds an M.D degree from Universidad Nacional Autónoma de México. He has medical specialties on General internal medicine, Cardiology, Nuclear cardiology and Positron emission tomography and Cardiac tomography.

**Jan Kybic** received the Master's degree from the Czech Technical University in Prague, Czech Republic and the PhD degree from EPFL, Switzerland, in 1998 and 2001, respectively. He held a postdoc position at INRIA, France, in 2002-2003. Since 2003, he has been at Czech Technical University in Prague, becoming an associate professor in 2010 and currently serving as a department head. He was a visiting researcher at EPFL for his sabbatical in 2010. He has authored or coauthored 21 articles in peer-reviewed international scientific journals, one book, two book chapters, and more than 60 conference publications. He has supervised 10 PhD students, five of them have already successfully graduated. He is an associate editor for the IEEE Transactions on Medical Imaging. His current research interests include algorithms for biomedical signal and image processing, especially image registration, segmentation and classification, numerical methods, interpolation, inverse problems, and algorithm theory.